Nanoscale

ROYAL SOCIETY OF CHEMISTRY

PAPER

View Article Online
View Journal | View Issue

Open Access Article. Published on 29 July 2022. Downloaded on 1/16/2026 11:38:56 AM.
This article is licensed under a Creative Commons Attribution-NonCommercial 3.0 Unported Licence.

Check for updates

Cite this: *Nanoscale*, 2023, **15**, 1145

GaAs/GaP superlattice nanowires: growth, vibrational and optical properties†

Omer Arif,[a] Valentina Zannier,[a] Francesca Rossi,[b] Diego De Matteis,[c] Katharina Kress,[c] Marta De Luca,[c,d] Ilaria Zardo[c] and Lucia Sorba*[a]

Received 29th April 2022,
Accepted 18th June 2022

DOI: 10.1039/d2nr02350d

rsc.li/nanoscale

Nanowire geometry allows semiconductor heterostructures to be obtained that are not achievable in planar systems, as in, for example, axial superlattices made of large lattice mismatched materials. This provides a great opportunity to explore new optical transitions and vibrational properties resulting from the superstructure. Moreover, superlattice nanowires are expected to show improved thermoelectric properties, owing to the dominant role of surfaces and interfaces that can scatter phonons more effectively, reducing the lattice thermal conductivity. Here, we show the growth of long (up to 100 repetitions) GaAs/GaP superlattice nanowires with different periodicities, uniform layer thicknesses, and sharp interfaces, realized by means of Au-assisted chemical beam epitaxy. By optimizing the growth conditions, we obtained great control of the nanowire diameter, growth rate, and superlattice periodicity, offering a valuable degree of freedom for engineering photonic and phononic properties at the nanoscale. As a proof of concept, we analyzed a single type of superlattice nanowire with a well-defined periodicity and we observed room temperature optical emission and new phonon modes. Our results prove that high-quality GaAs/GaP superlattice nanowires have great potential for phononic and optoelectronic studies and applications.

Introduction

Semiconductor nanowires (NWs) have been widely explored in recent years due to their peculiar properties and applications in a range of fields such as electronics and optoelectronics, and have become a vital part of the semiconductor technological roadmap.[1–5] In addition to homogeneous NWs, a large variety of NW heterostructures obtained with a modulation of either the chemical composition or the crystal structure have been demonstrated.[6–10] In particular, NW geometry allows for the coherent growth of lattice mismatched materials along the growth direction owing to the relaxation of elastic stress through the NW sidewalls,[11] offering a unique platform to explore material properties that are not achievable with conventional two dimensional (2D) counterparts. This is particularly interesting for the realization of superlattice (SL) structures, since the lattice mismatch strongly limited their development and consequent applications in the 2D form.

Within the class of III–V semiconductors, GaP plays a crucial role in modern photonics due to its wide transparency range (0.6–11 μm), high second-order nonlinear susceptibility, extremely low lattice mismatch with silicon, and a quasi-direct bandgap in a range of 2.18–2.25 eV when it is grown in the wurtzite (WZ) crystal structure.[12,13] Combining GaAs and GaP in a SL creates an outstanding material system for photonic and phononic applications.[14] In general, an alternation of two materials with different bandgaps can create electronic minibands and new optical transitions. Moreover, for phonon mean free paths comparable to SL periods, the periodic nature of the SL changes the phonon dispersion relation due to the interference of propagating phonons in the periodic structure.[15–17] This can enable the engineering of thermal conductivity, thus allowing improvements in the thermoelectric figure of merit of the material and the heat management in devices. Therefore, periodic and compositionally defined SLs are good candidates to investigate and control optoelectronic and thermal properties at the nanoscale.[18,19] However, the large lattice mismatch between GaP and GaAs (about 3.7%) strongly limits the layer thickness that can be obtained in planar SLs.[20] On the other hand, the NW geometry allows a higher degree of freedom in combining these materials with various layer thicknesses and periodicities. Moreover, the SL in

[a]NEST, Istituto Nanoscienze—CNR and Scuola Normale Superiore, Piazza San Silvestro 12, I-56127 Pisa, Italy. E-mail: lucia.sorba@nano.cnr.it
[b]IMEM—CNR, Parco Area delle Scienze 37/A, I-43124 Parma, Italy
[c]Physics Department, University of Basel, Klingelbergstrasse 82, CH-4056 Basel, Switzerland
[d]Physics Department, Sapienza University of Rome, P.le Aldo Moro 2, 00185 Rome, Italy

† Electronic supplementary information (ESI) available. See DOI: https://doi.org/10.1039/d2nr02350d

Open Access Article. Published on 29 July 2022. Downloaded on 1/16/2026 11:38:56 AM.
This article is licensed under a Creative Commons Attribution-NonCommercial 3.0 Unported Licence.

NWs allows advantage to be taken of unique optical effects typical of NWs, such as waveguiding, polarization-dependent absorption,[21,22] antenna effects,[23,24] and a more efficient phonon scattering.[25]

GaAs/GaP heterostructures in NWs have been poorly investigated so far, probably because of the polytype formation that typically occurs in such NWs[26] and the difficulty of controlling the crystal structure, growth rates,[27,28] and interface sharpness[29,30] in vapor–liquid–solid grown heterostructured NWs. Even if there are some reports on thin GaAs insertions (quantum dots) in GaP NWs,[30,31] the growth of regular GaAs/GaP SL NWs and their vibrational and optical properties have not been reported so far, to the best of our knowledge.

In this work, we achieved the growth of GaAs/GaP SL NWs, with different periodicities and uniform layer thickness within the entire structure, obtained by Au-assisted chemical beam epitaxy (CBE) on GaAs (111)B substrates. We varied different growth parameters such as Au film thickness, growth temperature, and growth time to study the morphology evolution of such NWs. We analyzed the NWs by scanning electron microscopy (SEM) and transmission electron microscopy (TEM), and we assessed their optical and vibrational properties by micro-photoluminescence (μ-PL) and micro-Raman spectroscopy, respectively. These indeed are powerful tools for the non-destructive study of material structural and optical quality.[32,33] For example, Panda *et al.* investigated the electronic band structure at the Γ point of defect-free WZ GaP NWs by resonance Raman spectroscopy.[34] De Luca *et al.*[16] studied the vibrational properties of twin SL GaP NWs by Raman spectroscopy and found specific phonon modes arising from the folding of the dispersion relation in the periodic superstructure. Maliakkal *et al.*,[35] Assali *et al.*,[36] and Da Silva *et al.*[12] measured the optical properties of pseudo-direct bandgap WZ GaP NWs by performing PL and PL-excitation spectroscopy.

Our results demonstrate that GaAs/GaP SL NWs with well-controlled periodicity and high structural and optical quality can be obtained by properly optimizing the growth conditions, paving the way to the use of this type of SL NW as a powerful platform for both fundamental investigations and device applications.

Results and discussion

As described in the Methods section, the growth protocol consisted of Au film annealing at 520 ± 5 °C, followed by a four-step growth process, namely step I: growth of the GaAs stem; step II: growth of the GaP segment; step III: growth of the GaAs/GaP SL; and step IV: growth of the top GaP segment. A schematic picture of the final NW structure can be found in Fig. 2a; however, we proceeded to analyze the NWs after each growth step, in order to realize uniform GaAs/GaP SL NWs. We first investigated the effect of Au film thickness on the length distribution of the GaAs stem and the GaP segment grown for 30 minutes (growth terminated after step II) as a function of nanoparticle diameter. SEM images of the samples obtained with the two different Au film thicknesses (0.1 or 0.5 nm) are presented in the ESI, section S1.† We found that a 0.1 nm thick Au film gives a much narrower length *vs.* diameter dispersion, as can be seen from the plot in Fig. 1a. The average values of the NW length and NP diameter are 1710 ± 95 nm and 42 ± 5 nm, respectively. In the case of a 0.5 nm thick Au film, instead, both length and diameter distributions are much broader, with average values of 1085 ± 313 nm and 55 ± 13 nm, respectively. The blue curve in Fig. 1a represents the dependence of L_{NWs} *versus* $(A + B/D_{NP})$, which is a clear signature that in this regime the growth is dominated by adatom diffusion.[37,38] Further data on the length distributions of the two samples can be found in the ESI, section S1.† Based on these results, we decided to use the 0.1 nm thick Au film for the growth of all the other samples in this work. Before proceeding with the growth of SL NWs with step III, we investigated the growth rate of the GaP segment (grown during step II) in this diameter range for different growth durations. In panel (b) of Fig. 1 we show a SEM image of the GaAs/GaP NWs with the GaP segment grown for 30 minutes. Full data for the different growth times are reported in the ESI, section S1.† We

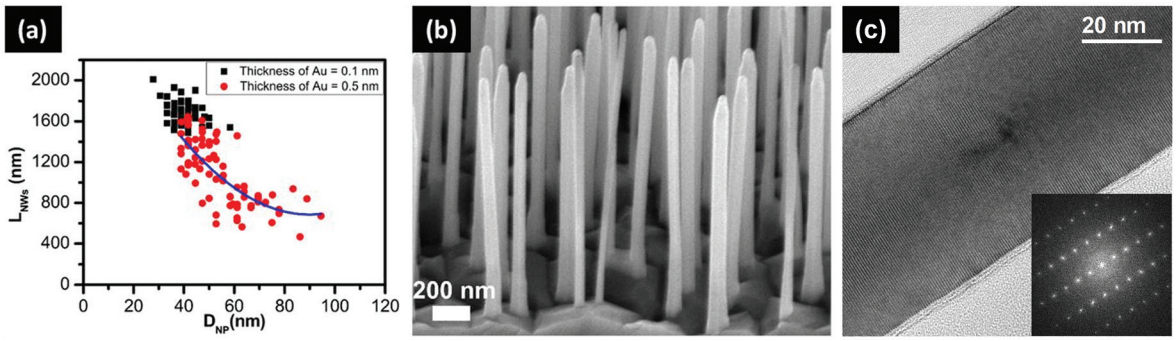

Fig. 1 (a) Length of nanowires (L_{NWs}) as a function of the diameter of the nanoparticle (D_{NP}) for two different Au film thicknesses: 0.1 nm (black squares) and 0.5 nm (red circles). The blue curve represents the $L_{NW} = A + B/D_{NP}$ fit. (b) A 45°-tilted SEM image of the GaAs/GaP NWs (growth stopped after step II) obtained with a 0.1 nm film thickness and 30 minutes of GaP growth time. (c) A HR-TEM image of the GaP portion of a representative GaAs/GaP NW oriented in the ⟨2-1-10⟩ zone axis, with its fast Fourier transform (FFT) as the inset.

 This journal is © The Royal Society of Chemistry 2023

Open Access Article. Published on 29 July 2022. Downloaded on 1/16/2026 11:38:56 AM.
This article is licensed under a Creative Commons Attribution-NonCommercial 3.0 Unported Licence.

found that the length distribution of the GaP segment is larger than that of the GaAs stem, and it broadens with an increase of the growth time. This broadening is consistent with a diffusion-driven growth mechanism.[39,40] However, the GaP axial growth rate is constant in this range, with an average value of 37 ± 3 nm min^{-1}.

Finally, we performed TEM measurements to investigate the crystal quality of the GaP segment. A representative TEM image is reported in panel (c) of Fig. 1 together with the FFT (inset). We found that the crystal structure of the GaP segment is WZ with very few stacking faults, consistent with that reported for these growth conditions,[41] and this result was reproduced in all the analyzed NWs.

After measuring the GaP growth rate and assessing the GaP crystal quality, we could grow thin GaAs and GaP alternating layers forming the SL (step III), and a long GaP top segment (step IV). Fig. 2a shows the schematics of the final structure. We grew samples with different layer thicknesses in the SL segment and number of repetitions from 30 to 100. Panel (b) of Fig. 2 shows a SEM image of the sample with a 1 μm long GaP stem, a 1 μm long GaP tip, and SL layer thicknesses of 3 nm of GaAs and 3 nm of GaP for 100 repetitions. In all the samples, we noticed that the average diameter of the NWs is always larger than the diameter of the GaAs stems and that of the GaAs/GaP NWs, indicating a significant radial growth occurring simultaneously with the axial growth. In order to understand this radial growth, we measured the diameter of the NPs (D_{NP}, blue triangles in Fig. 2c) and the diameter of the NWs 150 nm below the tip (D_{NW}, red circles in Fig. 2c) as a function of growth time. Different growth steps are marked with labels I, II, III, and IV and separated by dashed lines in Fig. 2c.

From the growth time evolution of D_{NP} and D_{NW} we observed that the nanoparticle diameter is constant, while the nanowire diameter is approximately the same for the GaAs stem and the bottom GaP segment (steps I to II), and it increases during the SL growth (step III) and remains large and constant during the GaP tip growth (step IV). As a result, we can conclude that a significant radial growth takes place during the growth of the SL segment. This occurs because of a reduced adatom diffusion during the SL growth that is probably due to the higher group V total pressure during the SL growth. In fact, radial growth originates from the nucleation and coalescence of islands on the sidewalls of the NW, similar to what occurs for conventional 2D growth at high V/III flux ratios.[42,43]

TEM analysis of a different SL sample, without the GaP top segment, allowed us to measure the real thickness and uniformity of each GaAs and GaP layer of the SL. Fig. 3a and b show the HAADF-STEM images of a representative GaAs/GaP SL with 30 periods of GaAs and GaP segments at different axial positions along the NW. The GaAs layers appear brighter than the GaP layers due to the presence of heavier As atoms. This contrast allowed us to measure the single layer thicknesses. In Fig. 3c we plot the thicknesses of all the GaAs and GaP layers of a NW with D_{NP} = 34 nm. The thickness mean values are also reported as a trend line for both materials, showing a good intra-wire thickness uniformity. We also investigated the thickness distribution for NWs of different diameters in the same sample, which resulted in 6.5 ± 0.5 nm and 8.0 ± 0.5 nm for GaAs and GaP, respectively. We can conclude that the growth conditions that we optimized allow us to obtain uniform inter-wire and intra-wire diameters, lengths, and SL periodicity.

Finally, we evaluated the interface sharpness. Panel (d) of Fig. 3 shows the STEM intensity profile obtained across a few SL layers near the NW tip, as indicated by the blue arrow in panel (b). We found that the GaP/GaAs interface is sharper (interface width ~15 Å) than the GaAs/GaP one (width up to 40 Å), as is visible by the different slopes. This has been reported also by other groups and it has been attributed to the

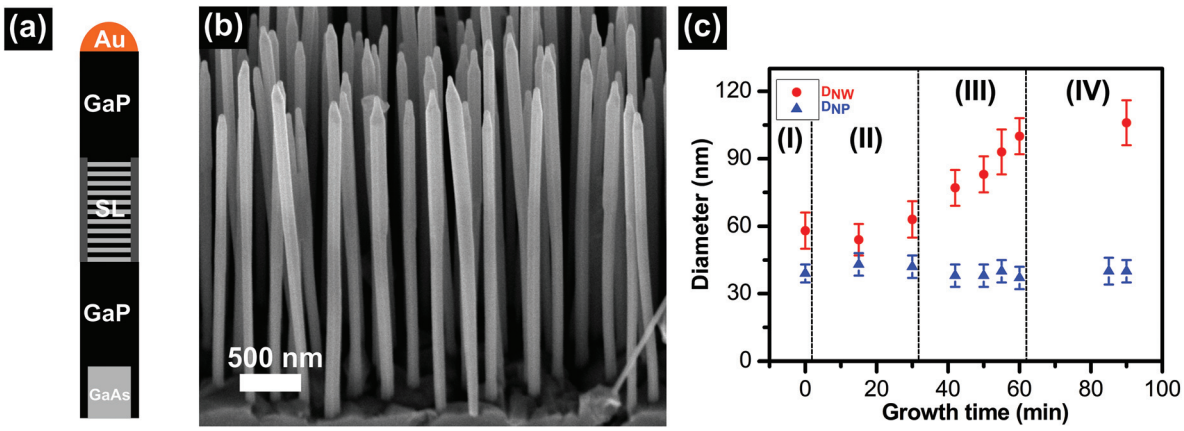

Fig. 2 (a) Schematics (not to scale) of the final structure of GaAs/GaP SL NWs (with only a few SL segments for simplicity). (b) A 45°-tilted SEM image of GaAs/GaP/SL/GaP NWs with layer thicknesses of 3 nm for GaAs and 3 nm for GaP in the SL. (c) Time evolution of D_{NW} and D_{NP}. The different steps of growth are delimited by dashed lines: the growth of the GaAs stem (step I), the growth of the GaP segment (step II), the growth of the GaAs/GaP SL (step III), and the growth of the top GaP segment (step IV).

Open Access Article. Published on 29 July 2022. Downloaded on 1/16/2026 11:38:56 AM.
This article is licensed under a Creative Commons Attribution-NonCommercial 3.0 Unported Licence.

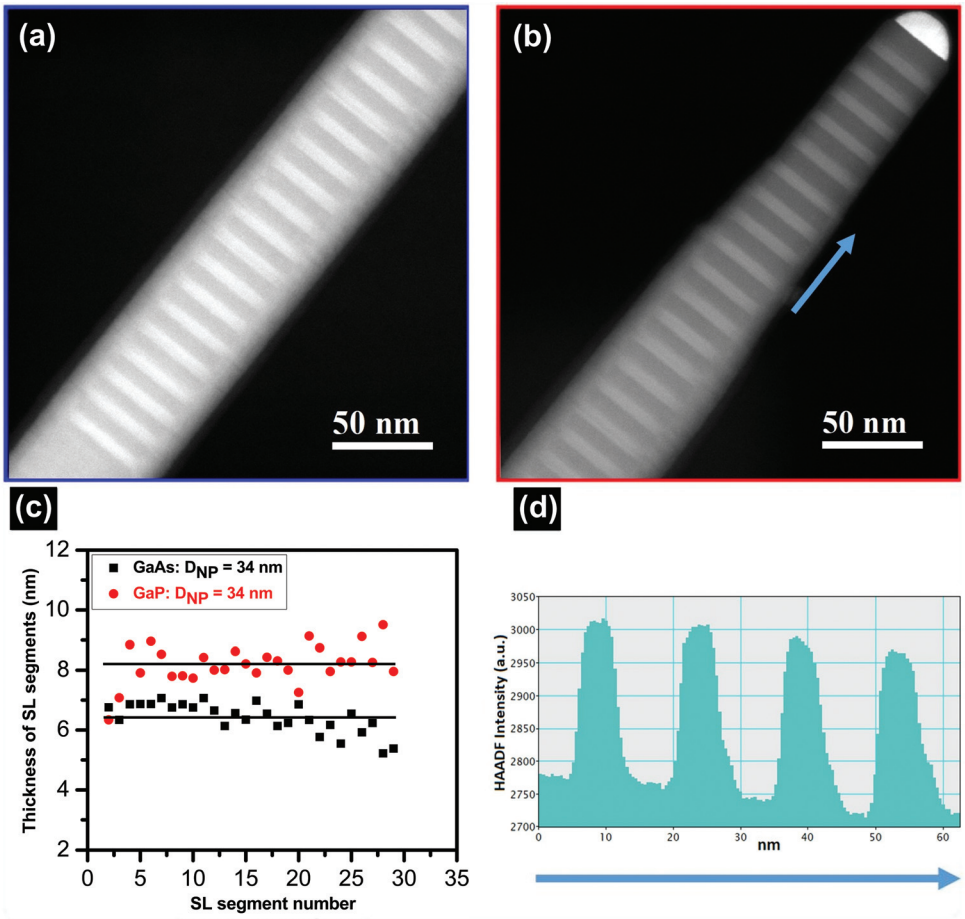

Fig. 3 TEM analysis of the GaAs/GaP SL NW. (a) and (b) HAADF-STEM images of the GaAs/GaP SL at the beginning and near to the NW tip, respectively. (c) A plot of the thickness of GaAs and GaP SL segments along the growth direction for a NW with D_{NP} = 34 nm. The lines represent the average thickness of GaAs (6.4 nm) and GaP (8.2 nm) segments. (d) STEM intensity profile along the blue arrow indicated in (b).

faster desorption of As than P from the NW sidewalls and a possible As incorporation at the beginning of the GaP layer growth.[29]

In order to investigate the lattice dynamics of the SL, we performed spatially resolved μ-Raman scattering experiments on a single GaAs/GaP/SL/GaP NW of the sample shown in Fig. 2a and b with the SL segment composed of 100 repetitions of a 3 nm GaAs layer alternated by a 3 nm GaP layer. A STEM analysis of a similar sample, without the GaP tip, confirmed the SL periodicity, as reported in section S2 of the ESI.† Fig. 4a presents a Raman micrograph of the NW, where the laser position of ~0.5 μm corresponds to the NW base and the laser position of ~4.25 μm corresponds to the NW tip. However, it is worth mentioning that the real length of the measured NW is smaller than the length measured by the Raman signal due to the finite laser spot size (0.5 μm).

The spectra were collected in a parallel polarization scattering configuration: both the polarization of excitation and detection were aligned parallel to the NW growth axis. We display the scattering intensity in false colors, as a function of both Raman shift (*x*-axis) and position along the NW (*y*-axis).

We observed distinct variations in the Raman signal along the NW axis, in terms of the number of features, their (relative) intensities and their frequencies. Overall, we observed three different types of spectra and their sequence is compatible with the GaAs/GaP SL NW structure sequence, as shown in Fig. 2a. Namely, from bottom to top we can distinguish a first region (0 μm to ~1.75 μm) with a high intensity Raman signal stemming from GaP (at ~363 cm^{-1}) and a low intensity GaAs-like signal (at ~270 cm^{-1}), followed by the SL segment (~1.75 μm to ~2.75 μm) with relatively strong intensity features between 270 and 290 cm^{-1} and between 360 and 400 cm^{1}, followed by a segment (~2.75 μm to ~4.25 μm) where only the Raman signal from GaP can be detected. A clear signal from the GaAs stem grown during step I, expected at 266 cm^{-1}, is absent, possibly because the NW was broken above this short segment during the transfer. The GaAs-like signal at ~270 cm^{-1} in the bottom part of the NW can be explained considering the GaAs radial growth occurring during step III, as explained above. This signal is indeed absent in the GaAs/GaP NWs (without SL), as shown in the ESI, section S3.†

Let us focus on the two spectra in Fig. 4b that we identify as the top GaP segment of the NW (black triangle) and the SL

 This journal is © The Royal Society of Chemistry 2023

Open Access Article. Published on 29 July 2022. Downloaded on 1/16/2026 11:38:56 AM.
This article is licensed under a Creative Commons Attribution-NonCommercial 3.0 Unported Licence.

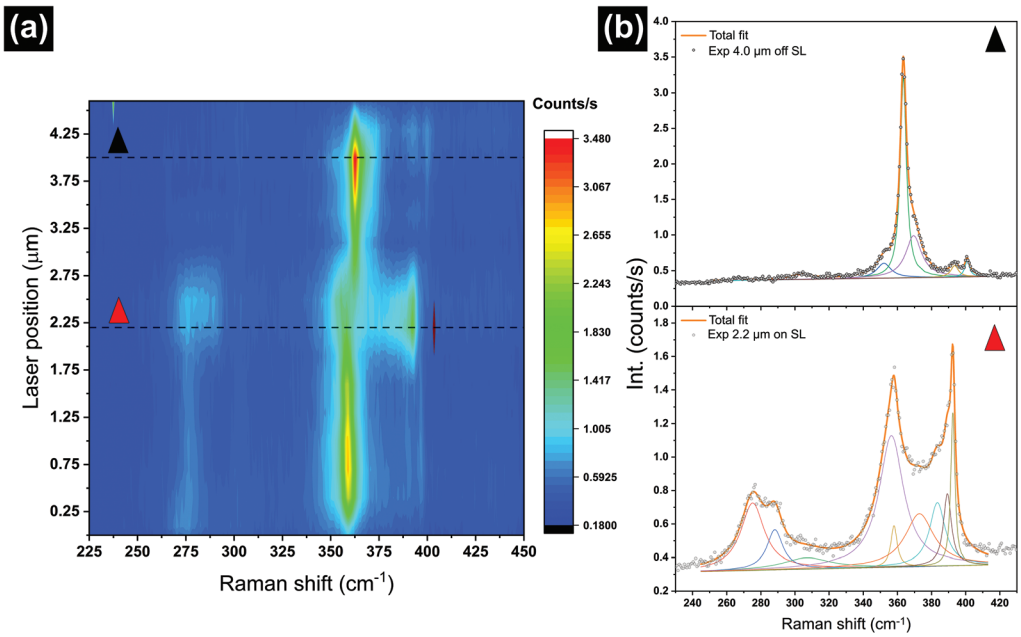

Fig. 4 μ-Raman microscopy of a 6 nm period of GaAs/GaP SL NW. (a) Scattering intensity (false colors) as a function of Raman shift (*x*-axis) and position along the NW (*y*-axis). Step size: 0.3 μm. (b) Two selected spectra from (a), as indicated by the dashed lines and the color of the triangles. The experimental data (symbols) are shown together with the individual deconvolution contributions (thin solid curves) and the cumulative fit (thick solid curves). The spectra come from the GaP top segment of the NW (top, black triangle) and from the SL segment (bottom, red triangle).

segment (red triangle). In the top one (black triangle) the deconvolution reveals that contributions are consistent with the spectrum of WZ GaP, with a very intense transversal optical (TO) mode at 362.7 cm^{-1} and a very low intensity longitudinal optical (LO) mode at 400.5 cm^{-1}.[44] Furthermore, two additional low intensity features can be observed as a result of the deconvolution of the spectrum at 352 and 393.3 cm^{-1}, which are stemming from the activation of the E_2^H mode and the surface optical (SO) mode, respectively, typical of the WZ phase and the NW morphology, respectively.[44,45] The bottom spectrum (red triangle) was collected at the position of the SL. By comparing the two spectra we observed three main changes: (I) a high-intensity GaP LO mode shifted at lower wavenumbers; (II) an increased signal between the TO and LO modes of GaP between 360 and 390 cm^{-1}; and (III) a relatively high intensity feature appearing between 270 and 285 cm^{-1}. All these three characteristics are peculiar and distinctive of the GaAs/GaP SL, due to the folding of phonon dispersion because of the reduced Brillouin zone size and to the change of the selection rules.[46] Indeed, the signature of a SL on the Raman spectrum can be understood as a result of the zone folding effect, a modification of the phonon dispersion due to the SL periodicity. Specifically, the presence of a SL induces a long-range periodicity in the crystal, which translates to a much smaller Brillouin zone in the reciprocal space with respect to the non-heterostructured crystal. This in turn results in the appearance of many minibands and, therefore, additional $k = 0$ phonon modes.[16,46–48] These additional phonon modes are responsible for the features between 270 and 285 cm^{-1} and between 360 and 390 cm^{-1}. We have performed a deconvolution of the spectra with Lorentzian curves using the least number of modes required for the fit to converge. This quantitative analysis should serve only as an indication of the frequencies of the phonons arising from the SL, as the individual SL modes cannot be resolved due to the limited spectral resolution. In order to confirm the interpretation of the Raman spectra, we also measured reference NWs without the SL, and the results are presented in the ESI, section S3.†

Finally, we performed μ-PL measurements on single NWs to investigate possible new emission bands associated with the presence of the SL and the optical quality of our samples. Room temperature μ-PL allows for detecting the intrinsic band-edge emission properties, such as the band gap energy, minimizing the contribution of defect states that dominate in low temperature measurements. Fig. 5a shows spatially resolved μ-PL measurements along the same GaAs/GaP SL NW shown in Fig. 4, while Fig. 5b shows the μ-PL spectra extracted from the scan in panel (a) at the two positions indicated by triangles. From position ~0 to ~1.8 μm and from ~2.7 to ~3.8 μm, the scan in panel (a) shows that almost no PL signal is detected, as can be better appreciated in the extracted spectrum in panel (b) (black triangle). This nearly zero PL intensity from the GaP segments below and above the SL (see the sketch in Fig. 2a) is consistent with the well-known very weak near-band-edge PL intensity of the WZ GaP NWs at room temperature, usually observed at ~1.9–2.2 eV and visible only when exciting with high power densities.[36] The PL signal from the GaAs stem, which would be expected from position 0 to ~0.5 μm at ~1.42 eV (namely the bandgap of GaAs NWs),[49,50]

Open Access Article. Published on 29 July 2022. Downloaded on 1/16/2026 11:38:56 AM.
This article is licensed under a Creative Commons Attribution-NonCommercial 3.0 Unported Licence.

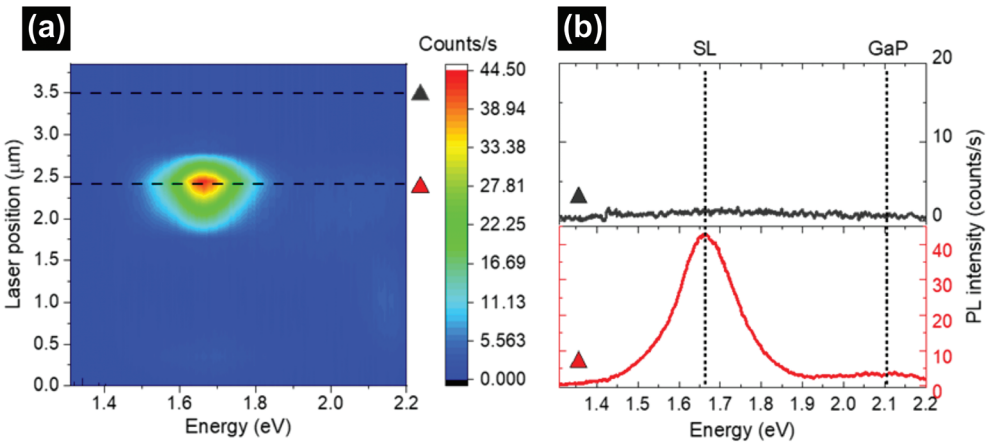

Fig. 5 (a) False color μ-PL map collected at room temperature and a power density of 13 kW cm^{-2} on the same NW investigated by Raman spectroscopy. The NW starts at 0 μm with a laser centered on the NW bottom (see the sketch in Fig. 2a) and ends at the NW tip at ~3.8 μm. Due to the absence of a significant signal outside the SL region, the first and last points of the map were collected with a laser fully positioned on the NW and not partially positioned on it as in the Raman map. This results in a PL map that is 700 nm shorter than the Raman map. The PL signal is detected only in the correspondence of the SL region. Dashed lines indicate the two NW positions from which the spectra shown in panel (b) are extracted. (b) Two selected spectra from (a), as indicated by the triangles. The spectra come from the SL segment (bottom, red triangle) and from the top GaP segment (top, black triangle). Dotted lines mark the center of mass of the two main spectral contributions: the SL band and the weak GaP-related band.

is also nearly zero, since the GaAs stem is likely absent in this NW, as discussed above. In section S4 of the ESI,† we provide additional PL measurements on other NWs, showing a GaAs-related band close to the NW bottom.

From position 1.87 to ~2.7 μm in Fig. 5a, we detected an intense PL band peaking at ~1.66 eV, as is also clear in the extracted spectrum in panel (b) (red triangle). The spatial dependence of this band suggests that it can be attributed to electronic transitions taking place in the GaAs/GaP SL region. In particular, the non-uniform intensity of this signal in the SL region (see variations from green to red color in the map) is due to the fact that the SL region is ~600 nm long (3 nm GaAs + 3 nm GaP, 100 repetitions), thus comparable to the PL laser spot size.

We point out that in strained planar GaAs/GaP SLs,[20] with the zinc blende crystal structure and period length about half of our SL period, a PL band at ~1.72 eV was observed at low temperature due to the type-II transition and a band at ~1.85 eV was observed at high temperature attributed to the type-I transition. The band we detected at RT at ~1.66 eV could thus be attributed to the type-I transition, where a different energy with respect to ref. 20 could be due to the different crystal structures, SL periods, and strains of our SLs, all parameters upon which the band structure largely depends. Another possible interpretation of the ~1.66 eV band would be the ground state of confined GaAs. Indeed, in ZB GaP NWs with embedded WZ GaAs QDs[31] and in ZB GaAsP NWs with embedded ZB GaAs QDs,[51] PL bands were reported in the range of 1.61 to 1.75 eV and attributed to confined GaAs in GaP barriers. However, in our SLs, the short period of both GaAs and GaP and the large number of repetitions (100) are more likely to give rise to a new band structure (to be investigated elsewhere).

In the extracted spectrum in Fig. 5b (red triangle), besides the SL band at ~1.66, we also detected a very weak GaP-related emission (at ~2.1 eV), while the GaAs-related emission is likely to be hidden by the intense SL band with which it partially overlaps, as shown in Fig. S4a†. These emissions could correspond to transitions that take place, respectively, in the separate pure GaP and pure GaAs layers of the SL. The reason why the GaP layers in the SL emit light while the bottom and top long GaP segments do not could be the quantum confinement taking place only in the SL, which localizes carriers in each segment and favors their recombination.

Finally, in order to confirm the attribution of the newly observed ~1.66 eV band in our SL NWs, we also collected μ-PL spectra of reference GaAs/GaP NWs without a SL segment, and of additional SL NWs (see the ESI, section S4†). In section S5 of the ESI,† we also show polarization dependent Raman and PL measurements, both confirming the WZ structure of these NWs.

Overall, these studies prove that while GaP NWs are well known to be poor light emitters at room temperature, our GaAs/GaP SL NWs are very good light emitters, comparable to state-of-the-art GaAs NWs. This intense signal confirms the very good optical quality of these SL NWs.

Conclusions

In conclusion, we found the optimal growth conditions to obtain long and highly uniform GaAs/GaP SL NWs with sharp interfaces, tunable layer thicknesses, and well-controlled SL periodicity. We carried out spatially resolved μ-Raman and μ-PL studies that allowed us to unveil the presence and the

 This journal is © The Royal Society of Chemistry 2023

Open Access Article. Published on 29 July 2022. Downloaded on 1/16/2026 11:38:56 AM.
This article is licensed under a Creative Commons Attribution-NonCommercial 3.0 Unported Licence.

precise location of the SL in single NWs. The μ-Raman studies revealed the presence of new phonon modes, arising from the SL due to the folding of the phonon dispersion. The intense PL signal observed at room temperature only on the short SL region proved that these SL NWs have great potential for optoelectronic applications. This work paves the way toward the possibility of manipulating the optical and vibrational properties of SL NWs at the nanoscale by using SL periodicity as a new degree of freedom.

Experimental section

Au-assisted GaAs/GaP SL NWs were grown on GaAs (111)B substrates by CBE in a Riber Compact-21 system. The metalorganic (MO) precursors used for the NW growth were triethylgallium (TEGa), tertiarybutylarsine (TBAs), and tertiarybutylphosphine (TBP). The GaAs (111)B substrates were first coated with a Au film with a nominal area-average thickness of 0.1 or 0.5 nm at room temperature in a KJL-thermal evaporator and then transferred to the CBE growth chamber. Prior to starting the growth process, the samples were annealed at 520 ± 5 °C under a TBAs flux for 20 min in order to dewet the Au film into nanoparticles and to remove the surface oxide from the GaAs substrate. The NW growth protocol consisted of four steps. In step I, the growth of a 0.5 μm long GaAs stem was performed for 60 min at 510 ± 5 °C using MO line pressures of 0.7 and 1 Torr for TEGa and TBAs, respectively. Afterward, the temperature was ramped up to 560 ± 5 °C in 5 min to initiate the growth of the GaP segment (step II) with a direct switch of the precursor fluxes without any growth interruption. The GaP segment was grown using MO line pressures of 0.7 and 2 Torr for TEGa and TBP, respectively. In step III, the growth of GaAs and GaP alternating segments forming the SL was performed at 560 ± 5 °C using the same MO line pressures. The SL contained from 30 to 100 periods with a repeating unit of GaAs and GaP segments with various nominal thicknesses, as indicated in the text above. Finally, (in step IV), a 1 μm long GaP top segment was grown by keeping unchanged the growth parameters (growth temperature and MO fluxes). The growth was terminated by switching off the TEGa flux and cooling the sample under a TBP flux. The NW morphology was characterized by SEM using a Merlin field emission microscope operated at 5 keV by acquiring top- and tilted-view (45°) images. From the tilted-view SEM images, we measured the following parameters for each sample: the diameter of a Au nanoparticle (D_{NP}), the NW diameter (D_{NW}), and the NW length (L_{NW}). All these quantities were averaged over ~50 NWs for each sample. The actual thickness of SL segments was determined by TEM using a JEOL JEM-2200FS microscope operated at 200 keV, equipped with an in-column Ω filter. Imaging was carried out in a high resolution HR-TEM mode combined with zero-loss energy filtering and scanning (STEM) mode using a high-angle annular dark-field (HAADF) detector yielding atomic-number (Z) contrast.

We carried out Raman microscopy measurements on single NWs (deposited on a Si substrate using a micromanipulator) by employing the 488 nm line of an Ar+ laser. We limited the power of the laser beam to 60 μW, in order to avoid damage to the sample and heating effects. The light was focused on the NW through a 100× Nikon objective with a numerical aperture of 0.95, resulting in a beam with a size of about 0.5 μm. The signal was collected in a backscattering configuration and analyzed using a T64000 Horiba triple spectrometer equipped with a liquid nitrogen-cooled CCD camera. Moreover, by implementing use of a half-wave plate and a polarizer on the excitation and detection lines, we performed polarization dependent measurements. The μ-PL measurements were performed at room temperature on the same NW investigated by Raman spectroscopy and using a similar power density. PL was excited by a diode-pumped laser (532 nm) using a 100× Zeiss objective with a numerical aperture of 0.75, resulting in a spot diameter of ~0.7 μm. The PL signal (collected in the backscattering configuration) was dispersed by a 0.5 m monochromator and detected with a liquid nitrogen-cooled CCD camera. The step size in the PL map was chosen to be half of the laser spot size, namely 350 nm.

Author contributions

O. A., V. Z., and L. S. grew the nanowires and measured the geometrical parameters, F. R. performed the TEM analysis, D. D. M., K. K. and I. Z. performed micro-Raman measurements, and M. D. L. performed micro-PL measurements. All authors have read and agreed to the published version of the manuscript.

Conflicts of interest

There are no conflicts to declare.

Acknowledgements

I. Z. acknowledges financial support from the European Research Council (ERC) under the European Union's Horizon 2020 research and innovation program (grant agreement no 756365). M. D. L. acknowledges support from the Swiss National Science Foundation (Ambizione Grant, PZ00P2_179801) and from the Italian Ministry of University and Research (Programma per Giovani Ricercatori "Rita Levi Montalcini").

References

1 H. J. Joyce, Q. Gao, H. Hoe Tan, C. Jagadish, Y. Kim, J. Zou, L. M. Smith, H. E. Jackson, J. M. Yarrison-Rice, P. Parkinson and M. B. Johnston, *Prog. Quantum Electron.*, 2011, **35**, 23–75.
2 M. Fang, N. Han, F. Wang, Z.-X. Yang, S. Yip, G. Dong, J. J. Hou, Y. Chueh and J. C. Ho, *J. Nanomater.*, 2014, **2014**, 1–14.

Open Access Article. Published on 29 July 2022. Downloaded on 1/16/2026 11:38:56 AM.
This article is licensed under a Creative Commons Attribution-NonCommercial 3.0 Unported Licence.

3 N. I. Goktas, P. Wilson, A. Ghukasyan, D. Wagner, S. McNamee and R. R. LaPierre, *Appl. Phys. Rev.*, 2018, **5**, 041305.
4 J. Wong-Leung, I. Yang, Z. Li, S. K. Karuturi, L. Fu, H. H. Tan and C. Jagadish, *Adv. Mater.*, 2020, **32**, 1904359.
5 K. Sarkar, P. Devi, K.-H. Kim and P. Kumar, *TrAC, Trends Anal. Chem.*, 2020, **130**, 115989.
6 O. Arif, V. Zannier, A. Li, F. Rossi, D. Ercolani, F. Beltram and L. Sorba, *Cryst. Growth Des.*, 2020, **20**, 1088–1096.
7 V. Zannier, F. Rossi, V. G. Dubrovskii, D. Ercolani, S. Battiato and L. Sorba, *Nano Lett.*, 2018, **18**, 167–174.
8 K. A. Dick, C. Thelander, L. Samuelson and P. Caroff, *Nano Lett.*, 2010, **10**, 3494–3499.
9 T. Burgess, S. Breuer, P. Caroff, J. Wong-Leung, Q. Gao, H. Hoe Tan and C. Jagadish, *ACS Nano*, 2013, **7**, 8105–8114.
10 S. Assali, L. Gagliano, D. S. Oliveira, M. A. Verheijen, S. R. Plissard, L. F. Feiner and E. P. Bakkers, *Nano Lett.*, 2015, **15**, 8062–8069.
11 F. Glas, in *Wide Band Gap Semiconductor Nanowires 1*, ed. V. Consonni and G. Feuillet, John Wiley & Sons, UK and USA, 2014, vol. 2, pp. 25–57. DOI: 10.1002/9781118984321.ch2.
12 B. C. da Silva, O. D. D. Couto Jr., H. T. Obata, M. M. de Lima, F. D. Bonani, C. E. de Oliveira, G. M. Sipahi, F. Iikawa and M. A. Cotta, *Sci. Rep.*, 2020, **10**, 7904.
13 S. Assali, I. Zardo, S. Plissard, D. Kriegner, M. A. Verheijen, G. Bauer, A. Meijerink, A. Belabbes, F. Bechstedt, J. E. Haverkort and E. P. A. M. Bakkers, *Nano Lett.*, 2013, **13**, 1559–1563.
14 M. S. Gudiksen, L. J. Lauhon, J. Wang, D. C. Smith and C. M. Lieber, *Nature*, 2002, **415**, 617.
15 C. Dames and G. Chen, *J. Appl. Phys.*, 2004, **95**, 682–693.
16 M. De Luca, C. Fasolato, M. A. Verheijen, Y. Ren, M. Y. Swinkels, S. Kolling, E. P. A. M. Bakkers, R. Rurali, X. Cartoixa and I. Zardo, *Nano Lett.*, 2019, **19**, 4702–4711.
17 M. N. Luckyanova, J. Garg, K. Esfarjani, A. Jandl, T. M. Bulsara, A. J. Schmidt, A. J. Minnich, S. Chen, M. S. Dresselhaus, Z. Ren, E. A. Fitzgerald and G. Chen, *Science*, 2012, **338**, 936–940.
18 J. Ravichandran, A. K. Yadav, R. Cheaito, P. B. Rossen, A. Soukiassian, S. J. Suresha, J. C. Duda, B. M. Foley, C. H. Lee, Y. Zhu, A. W. Lichtenberger, J. E. Moore, D. A. Muller, D. G. Schlom, P. E. Hopkins, A. Majumdar, R. Ramesh and M. A. Zurbuchen, *Nat. Mater.*, 2014, **13**, 168–172.
19 K. Shinokita, K. Reimann, M. Woerner, T. Elsaesser, R. Hey and C. Flytzanis, *Phys. Rev. Lett.*, 2016, **116**, 075504.
20 M. Recio, G. Armelles, J. Meléndez and F. Briones, *J. Appl. Phys.*, 1990, **67**, 2044–2050.
21 M. Y. Swinkels, A. Campo, D. Vakulov, W. Kim, L. Gagliano, S. E. Steinvall, H. Detz, M. De Luca, A. Lugstein, E. Bakkers, A. Fontcuberta i Morral and I. Zardo, *Phys. Rev. Appl.*, 2020, **14**, 024045.
22 M. De Luca, A. Zilli, H. A. Fonseka, S. Mokkapati, A. Miriametro, H. H. Tan, L. M. Smith, C. Jagadish, M. Capizzi and A. Polimeni, *Nano Lett.*, 2015, **15**, 998–1005.
23 R. Yan, D. Gargas and P. Yang, *Nat. Photonics*, 2009, **3**, 569–576.
24 G. Chen, J. Wu, Q. Lu, H. R. Gutierrez, Q. Xiong, M. E. Pellen, J. S. Petko, D. H. Werner and P. C. Eklund, *Nano Lett.*, 2008, **8**, 1341–1346.
25 R. Yan, D. Gargas and P. Yang, *Nat. Photonics*, 2009, **3**, 569–576.
26 J. P. Boulanger and R. R. LaPierre, *J. Cryst. Growth*, 2011, **332**, 21–26.
27 J. P. Boulanger and R. R. LaPierre, *J. Cryst. Growth*, 2014, **388**, 116–123.
28 M. A. Verheijen, G. Immink, T. De Smet, M. T. Borgström and E. P. A. M. Bakkers, *J. Am. Chem. Soc.*, 2006, **128**, 1353–1359.
29 M. T. Borgstrom, M. A. Verheijen, G. Immink, T. De Smet and E. P. A. M. Bakkers, *Nanotechnology*, 2006, **17**, 4010–4013.
30 G. Priante, G. Patriarche, F. Oehler, F. Glas and J. C. Harmand, *Nano Lett.*, 2015, **15**, 6036–6041.
31 P. Kuyanov, S. A. McNamee and R. R. LaPierre, *Nanotechnology*, 2018, **29**, 124003.
32 C. Fasolato, I. Zardo and M. De Luca, in *Fundamental Properties of Semiconductor Nanowires*, ed. N. Fukata and R. Rurali, Springer, Singapore, Singapore, 2021, pp. 307–348. DOI: 10.1007/978-981-15-9050-4_7.
33 A. Erbe, S. Nayak, Y. H. Chen, F. Niu, M. Pander, S. Tecklenburg and C. Toparli, in *Encyclopedia of Interfacial Chemistry*, ed. K. Wandelt, Elsevier, Oxford, 2018, pp. 199–219. DOI: 10.1016/B978-0-12-409547-2.14061-2.
34 J. K. Panda, A. Roy, M. Gemmi, E. Husanu, A. Li, D. Ercolani and L. Sorba, *Appl. Phys. Lett.*, 2013, **103**, 023108.
35 C. B. Maliakkal, M. Gokhale, J. Parmar, R. D. Bapat, B. A. Chalke, S. Ghosh and A. Bhattacharya, *Nanotechnology*, 2019, **30**, 254002.
36 S. Assali, J. Greil, I. Zardo, A. Belabbes, M. W. A. de Moor, S. Koelling, P. M. Koenraad, F. Bechstedt, E. P. A. M. Bakkers and J. E. M. Haverkort, *J. Appl. Phys.*, 2016, **120**, 0–10.
37 M. C. Plante and R. R. LaPierre, *J. Cryst. Growth*, 2006, **286**, 394–399.
38 V. G. Dubrovskii, G. E. Cirlin, I. P. Soshnikov, A. A. Tonkikh, N. V. Sibirev, Y. B. Samsonenko and V. M. Ustinov, *Phys. Rev. B: Condens. Matter Mater. Phys.*, 2005, **71**, 205325.
39 V. G. Dubrovskii, Y. Berdnikov, J. Schmidtbauer, M. Borg, K. Storm, K. Deppert and J. Johansson, *Cryst. Growth Des.*, 2016, **16**, 2167–2172.
40 Y. Berdnikov, A. A. Zhiglinsky, M. V. Rylkova and V. G. Dubrovskii, *J. Phys.: Conf. Ser.*, 2017, **917**, 032043.
41 E. Husanu, D. Ercolani, M. Gemmi and L. Sorba, *Nanotechnology*, 2014, **25**, 205601.
42 C. Chen, M. C. Plante, C. Fradin and R. R. LaPierre, *J. Mater. Res.*, 2011, **21**, 2801–2809.
43 M. C. Plante and R. R. LaPierre, *J. Appl. Phys.*, 2009, **105**, 114304.

 This journal is © The Royal Society of Chemistry 2023

Open Access Article. Published on 29 July 2022. Downloaded on 1/16/2026 11:38:56 AM.
This article is licensed under a Creative Commons Attribution-NonCommercial 3.0 Unported Licence.

44 R. E. Algra, M. Hocevar, M. A. Verheijen, I. Zardo, G. G. Immink, W. J. van Enckevort, G. Abstreiter, L. P. Kouwenhoven, E. Vlieg and E. P. Bakkers, *Nano Lett.*, 2011, **11**, 1690–1694.

45 R. Gupta, Q. Xiong, G. D. Mahan and P. C. Eklund, *Nano Lett.*, 2003, **3**, 1745–1750.

46 Z. V. Popovic, M. Cardona, E. Richter, D. Strauch, L. Tapfer and K. Ploog, *Phys. Rev. B: Condens. Matter Mater. Phys.*, 1990, **41**, 5904–5913.

47 B. Jusserand and M. Cardona, in *Light Scattering in Solids V*, ed. M. Cardona and G. Guntherodt, Springer, Germany, 1989, p. 79. DOI: **10.1007/BFb0051988**.

48 J. L. Merz Jr., A. S. Barker and A. C. Gossard, *Appl. Phys. Lett.*, 1987, **31**, 117.

49 M. De Luca, G. Lavenuta, A. Polimeni, S. Rubini, V. Grillo, F. Mura, A. Miriametro, M. Capizzi and F. Martelli, *Phys. Rev. B: Condens. Matter Mater. Phys.*, 2013, **87**, 1–8.

50 G. Signorello, E. Lortscher, P. A. Khomyakov, S. Karg, D. L. Dheeraj, B. Gotsmann, H. Weman and H. Riel, *Nat. Commun.*, 2014, **5**, 3655.

51 Y. Zhang, A. V. Velichko, H. A. Fonseka, P. Parkinson, J. A. Gott, G. Davis, M. Aagesen, A. M. Sanchez, D. Mowbray and H. Liu, *Nano Lett.*, 2021, **21**, 5722–5729.